



High-pressure melting line of helium from *ab initio* calculationsMartin Preising  and Ronald Redmer *Institut für Physik, Universität Rostock, D-18051 Rostock, Germany*

(Received 1 June 2018; revised manuscript received 16 July 2019; published 13 November 2019)

We applied two-phase simulations to directly calculate the high-pressure melting line of helium from 425 to 10 000 K and from 15 GPa to 35 TPa by using molecular dynamics based on density-functional theory. The implementation of the two-phase simulation method and the relaxation of the simulation to an equilibrium state was studied in detail, as well as its convergence with respect to particle number. We performed extensive two-phase simulations with the Perdew, Burke and Ernzerhof and the van der Waals density functional exchange-correlation functional and found almost identical results.

DOI: [10.1103/PhysRevB.100.184107](https://doi.org/10.1103/PhysRevB.100.184107)**I. INTRODUCTION**

Experimental data for the melting line of helium are currently available for pressures up to 80 GPa [1–7]. However, knowledge of the high-pressure melting line up to the TPa region is important to astrophysics, e.g., for the determination of the region of hydrogen-helium phase separation as predicted in the interior of gas giants like Saturn and Jupiter [8–12].

The phase diagram of solid helium was studied in depth in diamond anvil cell experiments. For instance, Mao *et al.* [13] observed a hexagonal close-packed (hcp) structure along the 300 K isotherm with x-ray diffraction experiments. Loubeyre *et al.* [14] extended the experimental range and detected a stable face-centered cubic (fcc) area embedded in the hcp structure at the melting line below 300 K.

Theoretical approaches for the calculation of the melting line start from the free energies of the solid (s) and liquid (l) phase in equilibrium and determine the melting point (p, T) from the equality of the corresponding Gibbs free energies, $G_l(p, T) = G_s(p, T)$, see Refs. [15,16].

An alternative method to determine the melting line directly is to treat the solid and the liquid in coexistence within two-phase simulations (TPSs). Pioneering work was performed by Belonoshko [17–20] and later by Alfè *et al.* [21] by combining a simulation box that contains a crystal with a box containing a liquid and subsequently relaxing the total system to an equilibrium state. When the number of atoms N , the simulation box volume V , and the internal energy E is fixed, the equilibrium pressure and temperature result in a point on the melting line, while the simulation box contains liquid and solid parts [22]. If the temperature is fixed, instead of the internal energy, the melting of the solid part of the box or the crystallization of the liquid part will occur. The location of the melting line can then be found in an iterative manner by changing the simulation parameters.

The first TPSs for helium were performed by Koči *et al.* [23] who reproduced the melting line as it was measured by Loubeyre *et al.* [4]. Belonoshko *et al.* [24] calculated the melting points of body-centered cubic (bcc) and fcc helium at about 14, 40, and 75 GPa with TPSs. The hcp phase was not considered. Nevertheless, the experimental melting line was

reproduced. The two studies employed classical molecular dynamics (MD) for the ions.

While the TPS method is very intuitive, its implementation poses several problems. For instance, a spacing between the solid and the liquid part is crucial to avoid particle overlap and excessive potential energies [23,25–27]. A possible starting point would be a crystal configuration in the simulation box at temperatures exceeding the melting temperature [28,29]. As soon as a liquid configuration is established, it is brought into contact with the initial crystal configuration. This implies a spacing of half of the lattice distance. To ensure density conservation, one or both parts of the supercell have to be compressed or expanded if the spacing is not equal to half of the lattice distance. However, a spacing of half of the lattice distance might not be enough to avoid excessive potential energies and could require other methods to achieve similar potential energies in the different phases of the supercell. For instance, one can remove atoms from the liquid part of the cell to equilibrate the pressure difference between the constituents [30]. In any case, the choice of the spacing is somewhat arbitrary. An alternative to the introduction of a spacing of an arbitrary size is the application of constant-pressure MD. Here, the size of the box in the direction orthogonal to the solid-liquid interface is allowed to change according to the pressure in the solid part.

Furthermore, there is no consensus on how both parts are to be set up in the first place. If a perfect crystal and a random liquid configuration are combined without previous relaxation, the results could be distorted. In some cases, the crystalline and the liquid part were relaxed prior to the TPS [22,27,30–32] and in some cases they were not [17,33,34].

References [27,35] performed tests on the influence of the joint surface plane and found no difference in the melting temperature, if the number of atoms is sufficiently large. Reference [24] performed calculations in which the solid part was either bcc or fcc. The experimental melting line was reproduced irrespective of the underlying solid structure that was simulated. This indicates that the influence of the crystal structure on the TPS results of helium is small in the temperature-density range that was examined in Ref. [24]. This is not necessarily the case for other densities and

temperatures. The influence of nuclear quantum effects (NQE) on the melting line was calculated by Ref. [36] and was found to be $\sim 5\%$ for high-pressure lithium. However, for systems with strong chemical bonds like hydrogen, the impact of NQE on the melting line can be significant, as Chen *et al.* [37] have demonstrated. Due to the very weak chemical bonds in helium, we chose to neglect NQEs.

Many calculations of the melting line [23,38–41] were performed with classical methods and empirical potentials. Young *et al.* [38] were the first to predict the melting line of helium up to temperatures of 6000 K. They employed linear muffin-tin orbital-calculations.

In this paper, we calculated the high-pressure melting line of helium with TPSs up to extreme pressures of 35 TPa and temperatures of 10 000 K. In particular, we studied how details in the setup of the simulation box for the TPS are affecting the results. As helium is a noble gas, it is very well suited for a case study, as there are no further chemical processes involved and the small number of electrons speeds up the electronic-structure calculations.

II. DFT-MD SIMULATIONS

In our simulations, we employed density-functional theory (DFT) [42,43] to treat the electrons, while the ions were propagated with classical MD. We used the implementation of the plane wave code VASP [44–48]. Due to the finite temperature, the electronic bands were occupied according to Fermi-Dirac statistics. The number of bands as well as the size of the time step were chosen individually for each temperature and density, as documented in Ref. [49]. A Nosé-Hoover thermostat [50–52] controlled the temperature of the ions.

To ensure a suitable choice of the pseudopotential, we performed static calculations of a perfect hcp helium crystal with 128 atoms and a random liquid configuration with 432 atoms with three different pseudopotentials: The standard projector-augmented wave (PAW) pseudopotential, [53] a “harder” PAW pseudopotential with a smaller cutoff radius than the standard one, and the full Coulomb potential. The Coulomb potential we employed for helium does not have a cutoff radius, in contrast to the PAW potentials. The cutoff energy corresponding to the Coulomb potential in this paper defines the number of plane waves that modeled the strongly oscillating wave functions around the nuclei. We assured convergence with respect to the number of plane waves for each of the potentials individually. The potentials require a maximum plane-wave energy (cutoff energy) of 800 eV (standard PAW), 2500 eV (harder PAW), and 15 000 eV (Coulomb) for a pressure convergence of better than 0.2% relative to calculations with cutoff energies of 3000 eV, 2500 eV, and 50 000 eV (PAW, harder PAW, and Coulomb, respectively). The harder PAW potential displayed a divergence of the internal energy above cutoff energies of 2500 eV. We therefore chose to discard the results that were obtained with higher cutoff energies. The Brillouin zone was sampled at the Baldereschi mean value point [54] (BMVP) for a cubic box (liquid) and with a $3 \times 3 \times 3$ \mathbf{k} -point set (hcp solid). The pressure of the hcp crystal and the pressure of the liquid are converged to within 0.1% with the respect to calculations with a $3 \times 3 \times 3$ and a $5 \times 5 \times 5$ \mathbf{k} -point set, respectively.

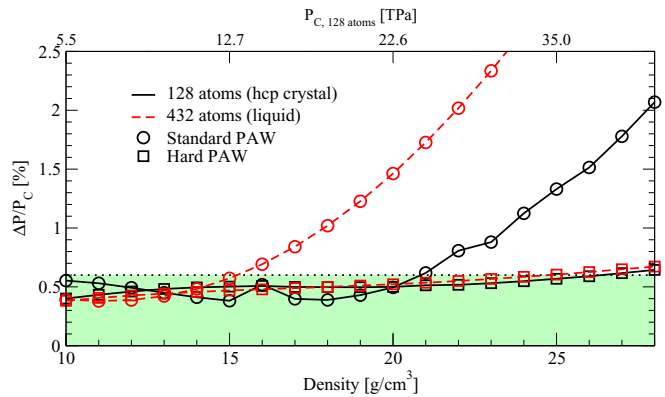


FIG. 1. Pressure deviations between the PAW pseudopotentials and the Coulomb potential. The pressure that was obtained for the perfect hcp crystal with the full Coulomb potential is shown on the upper x axis. The horizontal dotted line guides the eye.

The exchange-correlation (XC) functional was Perdew, Burke and Ernzerhof (PBE) [55] in all convergence tests. For these tests, we chose high densities to ensure the convergence of the Coulomb potential, which is very demanding at lower densities. The density region under consideration is also the region in which the PAW pseudopotentials are expected to give unphysical results as soon as the interatomic distance approaches the cutoff radius [56]. Figure 1 shows the pressure deviations ΔP between the pseudopotentials relative to the pressure P_C that was obtained with the Coulomb potential. As Lorenzen [56] demonstrated, the forces on the ions are converged when the resulting pressures are converged.

The correspondence of the standard PAW potential with the full Coulomb potential is better than 0.6% at densities up to 15 g/cm^3 . The hard PAW potential reproduces the pressure obtained with the Coulomb potential within 0.6% for densities below 25 g/cm^3 . For densities below 14 g/cm^3 , we utilized the standard PAW potential with an energy cutoff of 900 eV and switched to the harder PAW potential with an energy cutoff of 2500 eV for densities of 14 g/cm^3 and above. Only the PBE calculations of the melting point at 10 000 K exceed 24 g/cm^3 and are therefore converged to within 0.65%. Therefore, we utilized only the standard and the hard PAW potential.

When we decrease the size of the simulation box, the size of the cell in reciprocal space increases. Therefore, a Brillouin zone sampling that is sufficient at low densities might not be at very high densities. We studied densities from 1 to 30 g/cm^3 and analyzed the convergence of a perfect hcp crystal with 128 atoms. We switched to the hard PAW potential at densities higher than 14 g/cm^3 . The pressures of the calculations with the perfect hcp crystal are converged to within 0.4% with the BMVP compared to $5 \times 5 \times 5$ for all the densities under consideration.

III. TWO-PHASE SIMULATIONS

To ensure fully converged TPS results, we performed extensive test calculations, mostly for a density of 1.6 g/cm^3 . At this density, the PBE XC functional results in pressures below 80 GPa in the temperature range in which experimental

data [7] for the melting line of helium are available. We also verified the convergence of the TPS calculations at 17 and 20 g/cm³. Please note that we did not relax the cell shape but employed the perfect c/a ratio. When we relaxed the cell at the lowest and the highest density, the box vectors were identical to the perfect ones within 2.2%. This resulted in pressure deviations of less than 0.16% between the relaxed and the perfect hcp cells. This deviation is negligible. As discussed in Sec. II, the forces on the ions are converged if the pressures are converged.

A. Setup of the simulation box

Our setup scheme was similar to that of Ref. [30]. To set up the solid subdomain before the TPS was performed, we chose a temperature T_s of around 70% of the experimental melting temperature. At this temperature, a perfect hcp crystal was relaxed for 5 ps. The resulting atomic configuration and its velocity vectors were used as the input for the next calculation, in which the crystal was heated with a rate of 50 K/ps until melting occurred at T_s^m . After every picosecond of this heating process, the ionic positions and the corresponding velocity vectors were recorded. Every snapshot was then further relaxed at its respective temperature for an additional 2 ps.

In the exact same manner, the ionic configuration and velocity vectors of the liquid subdomain were obtained as the result of a relaxation at a temperature T_l above the experimental melting temperature followed by a cooling procedure with a rate of 50 K/ps until the starting temperature of the solid was reached. The resulting snapshots were relaxed for 2 ps.

From the ionic configurations and their velocity vectors, the TPS boxes were constructed. The results of the setup procedure depicted above were TPS boxes at a density of 1.6 g/cm³ and temperatures between T_s and T_s^m or T_l , depending on which is lower. The temperature difference between these TPS boxes is 50 K. The interface of the solid and the liquid phase was [0001]. References [27,35] found that the influence of the joint surface plane is negligible provided that the number of atoms is sufficient (96 atoms in Ref. [27], 108 atoms in Ref. [35]). We therefore chose not to perform tests on the joint interface plane.

The problem of excess potential energies at the construction of the TPS boxes can be avoided by using three methods. The first method employs constant pressure MD during the TPS. In this method, the shape of the liquid part of the box can change in the direction perpendicular to the interface. The second method evaluates the pressure of the solid part and removes atoms from the liquid part until the pressures of both parts are comparable. Then the boxes are brought into contact and the TPS is conducted with a spacing of half the lattice distance between the constituents. We call this method *equilibrated TPS (e-TPS)*. However, with this method, the formation of a crystal without defects is not possible due to the fact that there are atoms missing. The third method compresses the solid in such a way that the excess pressure of the liquid is compensated. We call this method *compressed TPS (c-TPS)*. These methods can also be combined by relaxing the liquid and the solid part prior to the compression of the solid part. We call this *compressed relaxed TPS (cr-TPS)*.

The TPS boxes were simulated in the NVT ensemble until the crystal melted or the liquid froze. These processes were monitored with the radial distribution function, the mean-square displacement, the pressure, and internal energy during the simulation, and direct visualization of the atomic configurations with the visual molecular dynamics tool [57].

B. Influence of the atom number

As solid helium exists in an hcp structure [13] in the regime we are interested in, the number of atoms for the crystal is restricted to $2n^3$, where n is the number of periodic images of the unit cell per space dimension. The TPS cells with 256 atoms were obtained with four unit cells in every direction in the solid and the liquid, respectively. In the same way, the TPS box with 500 atoms was constructed from five unit cells in every direction and the box with 864 atoms from six unit cells in every direction. Note that due to the hcp basis cell, the box is not cubic. We did not relax the cell parameters prior to the TPS calculations, as mentioned above. By applying the heating/cooling scheme as described above with just 54 atoms in the box, the liquid crystallized at 1300 K, while the crystal melted above 1100 K. As there was no temperature overlap in which we could perform TPS, we concluded that the number of 54 atoms for each constituent and 108 in the TPS is not sufficient. We achieved a sufficient temperature overlap with 128 and more atoms and calculated the melting temperature with 256, 500, and 864 atoms in the TPS box with the setup procedure as it was described above for cr-TPS. The c-TPS ansatz, i.e., a compressed perfect crystal and a random liquid configuration in the simulation cell, was tested with 256, 500, 864, and 2048 atoms in the simulation cell, as well as the e-TPS ansatz with 254, 495, and 856 atoms, see Fig. 2. We employed a \mathbf{k} -point sampling at the Γ -point and performed additional calculations with a \mathbf{k} -point at 0 1/3 0 and a Monkhorst-Pack set of $2 \times 2 \times 2$.

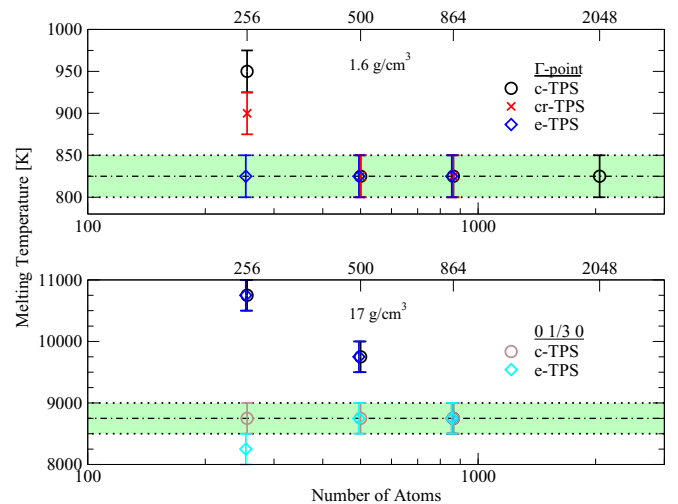


FIG. 2. Convergence of the melting temperature with respect to the number of atoms at a density of 1.6 and 17 g/cm³. Shown are results for c-TPS (circles), cr-TPS (crosses), and e-TPS (diamonds). The lower panel demonstrates the necessity to change the \mathbf{k} -point sampling at higher densities, see the discussion below.

For the calculations at 1.6 g/cm^3 , we can see systematic behavior of the c-TPS and the cr-TPS. The e-TPS seems to be converged with 254 atoms already. The convergence of the different TPS methods with respect to the number of atoms is consistent with the results of Refs. [30,34,37]. At 17 g/cm^3 , a \mathbf{k} -point sampling at the Γ -point is not sufficient for converged TPS calculations with 500 atoms. Instead, a more precise sampling has to be employed.

The smaller the number of atoms in the simulation box, the higher the impact of the initial velocity vector distribution. With an increasing number of atoms, the crystal lattice becomes more and more stable as the random lattice errors induced by the velocity vector initialization average out. We therefore concluded that 500 atoms are sufficient to obtain well-converged results irrespective of the TPS method. We chose c-TPS, which drastically simplifies the setup procedure compared to the cr-TPS and the e-TPS scheme. The latter was also employed by Ref. [30].

The simulation box of the TPS configuration is a hcp cell that is elongated in the z-direction. The intuitive choice of a \mathbf{k} -point sampling has less \mathbf{k} -points in the direction of the elongation. When we employ a sampling of $2 \times 2 \times 2$ (12 \mathbf{k} -points) or better, the maximum deviations in pressure between those more accurate samplings are within the numerical noise. Some special points in the Brillouin zone of the hexagonal cell, given by Ref. [58], result in a pressure convergence of better than 0.05% over a density range of 1 to 30 g/cm^3 compared to the more demanding sampling mentioned above. For the TPS, we employ the Γ -point for densities below 7 g/cm^3 and a \mathbf{k} -point at $0 \frac{1}{3} 0$ in reciprocal space for higher densities.

For a density of 17 and 20 g/cm^3 , we studied the influence of the choice of the pseudopotential as well as the choice of \mathbf{k} -point sampling. As described above, we expected a significant difference between the standard and the hard PAW potential above 14 g/cm^3 . However, when we calculated the melting temperature at 20 g/cm^3 with a \mathbf{k} -point sampling at the Γ -point, a Monkhorst-Pack set of $2 \times 2 \times 2$, and a \mathbf{k} -point at $0 \frac{1}{3} 0$, we obtained no difference between the pseudopotentials. The corresponding melting temperatures at 20 g/cm^3 were $10\,750 \pm 250 \text{ K}$ for the Γ -point calculations and $9750 \pm 250 \text{ K}$ with the \mathbf{k} -point at $0 \frac{1}{3} 0$ and $2 \times 2 \times 2$. The respective melting temperatures at 17 g/cm^3 were 1000 K lower than those at 20 g/cm^3 . Again, the melting points obtained with the hard PAW potential and a Monkhorst-Pack set of $2 \times 2 \times 2$ result in the same melting temperature as the standard PAW potential and a single \mathbf{k} -point at $0 \frac{1}{3} 0$ at high densities. We therefore employ the standard PAW potential throughout this study for the TPS calculations, except for the melting points at $10\,000 \text{ K}$ that exceeded 20 g/cm^3 . Here, we employed the hard PAW potential for the TPS calculations.

C. Influence of the spacing

In the considered region of the helium phase diagram, the pressure in a liquid part is greater than that in a solid part, if the box volume and temperature are equivalent. This causes the atoms of the liquid part of the TPS box to expand into the solid, which subsequently begins to melt, if no spacing between the constituents is introduced. To circumvent this

well-known problem, we compressed the crystal in such a way that the liquid part was attached to the solid at a certain fraction of the lattice distance $b = a\sqrt{3}/2$. Here, a is the smaller lattice constant of an hcp lattice. The compression increases the pressure in the solid. At the beginning of the TPS, the excess pressures in each part of the box are decreased by the expansion of both parts into the void between them. To benchmark the influence of the spacing size on the result, we set up TPS boxes with 500 atoms and identical liquid and solid parts but different fractions of b from 95% to 108%. Each of these TPS boxes was then simulated with the PBE XC functional at 7000 K and densities of 9.70, 9.88, 9.92, 9.96, 10.00, 10.04, 10.08, 10.12, 10.30, 10.47, and 10.54 g/cm^3 . We found no dependency of the results on the spacing. However, at the greatest and the smallest spacings under consideration and therefore a smaller or bigger compression of the solid part, the solid part showed increasing oscillations perpendicular to the interface. We limited our calculations to parameters in which this unphysical behavior did not occur. We found that as long as the spacing size is within this range, the choice of b is arbitrary. We chose a spacing of 100%. The liquid part is therefore attached to the solid part where the next crystal plane would be in the compressed solid.

D. Influence of the metastable region

The melting of a solid is a first-order phase transition. When we performed TPS calculations at various densities, we encountered a region of higher density in which all TPS calculations yielded solid results and a region of lower density in which all TPS calculations gave liquid results. The density region in between is metastable and can result in either a solid or a liquid. The sampling of this metastable region was a byproduct of the study of the influence of the spacing. The simulations demonstrated that the mean size of the metastable region is 3.4% in density. We therefore infer a typical error of 3.5% in density for the EOS calculations that follow the TPS, see Sec. IV. This statistical behavior can be utilized to resolve the pressure and temperature during the melting transition with fewer atoms but a greater number of TPS simulations [35].

The final TPS calculations were performed with 500 atoms, a spacing of b , a Brillouin zone sampling with the Γ point at densities below 7 g/cm^3 , and with a \mathbf{k} -point at $0 \frac{1}{3} 0$ for higher densities, and with the PBE and the van der Waals density functional (vdW-DF1) [59] XC functionals to be consistent with recent hydrogen-helium demixing calculations [12,60,61]. As Monserrat *et al.* [62] found the hcp structure to be the most stable at pressures between 10 and 20 TPa and no contradicting experimental results nor other predictions from random structure search algorithms exist, we assumed solid helium to remain in the hcp structure throughout the entire pressure range considered here, i.e., from 15 GPa to 35 TPa. However, the extreme high-pressure phase of helium is considered to be bcc. [63] The TPS results of Belonoshko *et al.* [24] that were obtained with the fcc and bcc structure are in good agreement with the experimental melting line, where the underlying crystal structure is hcp. This indicates that the underlying crystal configuration might not be essential for the

reproduction of the helium melting line, at least in the part of the phase diagram that was investigated by Ref. [24].

IV. CALCULATION OF THE MELTING LINE

The high number of atoms that is required for converged TPSs is neither necessary nor computationally feasible for converged pressures as the pressure obtained with 128 atoms is identical to the pressure with a greater number of atoms within 0.15%. The pressure inside a TPS box drops if the resulting phase is solid, but several thousand additional time steps would be required for the pressure to fluctuate around the solid equilibrium pressure at the given density and temperature T . The same applies for rising pressures and liquid TPS results. To save computation time, we performed calculations of the solid or liquid phase with 128 atoms for at least 5 ps. To ensure the integrity of the hcp structure, we heated a perfect hcp crystal within 5 ps from a temperature of $0.8T$ to T prior to the relaxation process described above. However, the densities at which converged pressures were calculated with 128 atoms are the result of TPS with 500 atoms.

As discussed above, the lowest possible solid density at a given temperature cannot be determined exactly with TPS. Therefore, we made a conservative estimate of an error of 3.5% in density based on the results of Sec. III. First, we performed TPS simulations on a density grid with a width of less than 2% for every temperature under consideration. Then, the pressure P_s of the lowest density ρ_s at which the TPS results in a solid at a given temperature was calculated with 128 atoms, as well as the pressure P_l that corresponds to the highest density with a liquid TPS result and $\rho_l < \rho_s$. The mean pressure $|P_s - P_l|/2$ yielded the melting pressure p_m .

To account for the uncertainties due to the density jump along the first-order phase transition, we also calculated the pressure of a solid at a density that is 3.5% smaller than ρ_s . The pressure deviation of the two solid configurations is the uncertainty we added to the pressure difference $|P_s - P_l|$ to estimate the error of the melting pressure p_m , as discussed above. We chose to perform the calculations at constant temperatures to provide the melting points at the exact temperatures that were required by Ref. [12]. The solid pressures were calculated in a hexagonal cell, while the pressures of the liquid were obtained with cubic simulation boxes.

The algorithm for the calculation of one point of the melting line can be summarized as follows:

- (i) At a fixed temperature, iteratively find the density where melting occurs with 500 atoms and TPS until the difference in density between the least dense solid ρ_s and the most dense liquid result ρ_l is $< 2\%$.
- (ii) Calculate the pressures P_s and P_l corresponding to ρ_s and ρ_l with 128 atoms.
- (iii) Calculate the pressure P'_s corresponding to $\rho'_s = 0.965\rho_s$ with 128 atoms.
- (iv) Calculate the melting pressure $P_m = (P_s + P_l)/2$.
- (v) Calculate the error in pressure $dP_m = |P'_s - P_s|$.

The final results for the high-pressure melting line of helium obtained with TPSs are displayed in Fig. 3.

The different XC functionals resulted in the same melting line within the error bars and reproduced the available experimental data very well. The vdW-DF1 functional resulted

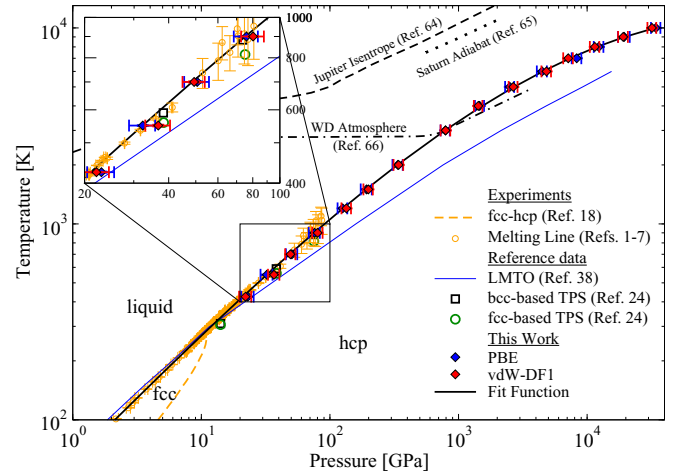


FIG. 3. Helium phase diagram with the TPS results (diamonds) that employed the PBE (blue) and vdW-DF1 (red) XC functional compared with experimental data (orange) [1–7]. Note that we plotted the data of Ref. [7] as corrected by Ref. [24]. The previous melting line predictions (blue line, black squares, and red circles) [24,38], the coldest Jupiter adiabat of the preliminary Jupiter model of Hubbard and Militzer [64], the coldest possible adiabatic layer of helium around Saturn’s core of Püstow *et al.* [65], and the coldest P-T profile of white dwarfs of Ref. [66] are displayed as well. The inset shows a magnification of the melting line between 400 and 1000 K. The fit function to our TPS results is depicted as a bold black line.

in systematically lower densities for the melting points than the PBE functional at the same temperature. However, the vdW-DF1 functional also yielded higher pressures than the PBE functional at the same density and temperature. These two effects canceled each other out, which resulted in identical pressures within the error bars. Different XC functionals can give different pressures at identical densities due to the construction of the XC functionals and their parameters, respectively. The enhancement factor of revPBE, the exchange functional that underlies vdW-DF1, over the reduced gradient has a steeper slope than that of PBE. This results in a stronger repulsion of the ions and therefore in higher pressures, see Ref. [67]. The TPS melting line lies above the linear-muffin-tin-orbital results of Ref. [38]. The melting line shows a slight downward curvature at higher pressures but not as pronounced as was predicted by Young [38].

In Saturn and possibly Jupiter, the demixing of hydrogen and helium into a helium-rich and a helium-poor component might act as an additional heat source, which could explain the high luminosity of Saturn [8–10,12,60,65]. The accurate location of the melting line of helium is relevant to the helium-rich side of the miscibility diagram of hydrogen and helium, in particular when the demixing temperatures approach the helium melting line for high helium concentrations [12]. Note that our melting line is located well below the isentropes of Jupiter [64] and Saturn [65]. Therefore, if a helium-rich layer is formed due to H-He demixing, it is still liquid. Prior to our investigations, the possibility of solid helium in the giant planets of the solar system could not be estimated. Models of very old and cool white dwarf atmospheres that consisted of pure helium [66] predicted a P-T profile that intersects

our TPS melting line. This is important for accurate interior models of white dwarfs. The knowledge of the melting line paves the way for consistent wide-range equation of states calculated with DFT-MD like the He-REOS.3 [68], which can be applied in planetary physics.

We could not find a Simon-Glatzel [69] or Kechin equation [70] that reproduces all of the experimental data as well as our averaged TPS results with $p(T)_{\text{Melt}} = (p(T)_{\text{Melt, PBE}} + p(T)_{\text{Melt, vdW-DF1}})/2$. Therefore, we chose a fit function of the type

$$T(P) = \exp[a + b \ln P + c(\ln P)^2 - d(\ln P)^3], \quad (1)$$

with $a = 4.11633$, $b = 0.649134$, $c = 4.13856 \cdot 10^{-5}$, and $d = 1.48182 \cdot 10^{-3}$. The Kechin equation of Ref. [7] predicts an upward curvature of the melting line in Fig. 3, which is not reproduced by our TPS results. Please note that we therefore did not include the data of Ref. [7] in the fitting procedure.

V. CONCLUSION

We calculated the high-pressure melting line of helium with the two-phase approximation with DFT-MD by using the PBE and the vdW-DF1 XC functional. The different function-

als resulted in the same melting line within the error bars. The results for the experimental melting line up to 100 GPa were reproduced. The calculations span a temperature range of one magnitude and a pressure range of three magnitudes, i.e., from 425 K to 10 000 K and from 15 GPa to 35 TPa. We find that the high-pressure melting line exhibits a slight downward curvature. The implementation of the TPS cell and the calculation of the melting pressure in this paper were developed to minimize the computational effort that is required for the setup procedure of the TPS cell and the calculation of the melting pressure. Its general applicability has to be demonstrated.

ACKNOWLEDGMENTS

We thank M. French, C. Kellermann, N. Nettelmann, M. Schöttler, and F. Tomm for helpful discussions and remarks. We thank the anonymous referees for helpful comments. This work was supported by the Deutsche Forschungsgemeinschaft within the Sonderforschungsbereich 652, by the North German Supercomputing Alliance (HLRN) and the ITMZ of the University of Rostock.

-
- [1] J. S. Dugdale and D. K. C. MacDonald, *Phys. Rev.* **89**, 832 (1953).
 - [2] R. K. Crawford and W. B. Daniels, *J. Chem. Phys.* **55**, 5651 (1971).
 - [3] R. L. Mills, D. H. Liebenberg, and J. C. Bronson, *Phys. Rev. B* **21**, 5137 (1980).
 - [4] P. Loubeyre, J. M. Besson, J. P. Pinceaux, and J. P. Hansen, *Phys. Rev. Lett.* **49**, 1172 (1982).
 - [5] W. L. Vos, M. G. E. van Hinsberg, and J. A. Schouten, *Phys. Rev. B* **42**, 6106 (1990).
 - [6] F. Datchi, P. Loubeyre, and R. Le Toullec, *Phys. Rev. B* **61**, 6535 (2000).
 - [7] D. Santamaría-Pérez, G. D. Mukherjee, B. Schwager, and R. Boehler, *Phys. Rev. B* **81**, 214101 (2010).
 - [8] D. J. Stevenson, *Phys. Rev. B* **12**, 3999 (1975).
 - [9] D. J. Stevenson and E. E. Salpeter, *Astrophys. J. Suppl. Ser.* **35**, 221 (1977).
 - [10] J. J. Fortney and W. B. Hubbard, *Astrophys. J.* **608**, 1039 (2004).
 - [11] J. J. Fortney, *Science* **305**, 1414 (2004).
 - [12] M. Schöttler and R. Redmer, *Phys. Rev. Lett.* **120**, 115703 (2018).
 - [13] H. K. Mao, R. J. Hemley, Y. Wu, A. P. Jephcoat, L. W. Finger, C. S. Zha, and W. A. Bassett, *Phys. Rev. Lett.* **60**, 2649 (1988).
 - [14] P. Loubeyre, R. LeToullec, J. P. Pinceaux, H. K. Mao, J. Hu, and R. J. Hemley, *Phys. Rev. Lett.* **71**, 2272 (1993).
 - [15] D. Alfè, L. Vočadlo, G. Price, and M. Gillan, *J. Phys.: Condens. Matter* **16**, S973 (2004).
 - [16] G. Robert, P. Legrand, P. Arnault, N. Desbiens, and J. Clérouin, *Phys. Rev. E* **91**, 033310 (2015).
 - [17] A. B. Belonoshko, *Geochim. Cosmochim. Acta* **58**, 4039 (1994).
 - [18] A. B. Belonoshko and L. S. Dubrovinsky, *Geochim. Cosmochim. Acta* **59**, 1883 (1995).
 - [19] A. Belonoshko and R. Ahuja, *Phys. Earth Planet. Inter.* **102**, 171 (1997).
 - [20] A. B. Belonoshko, R. Ahuja, and B. Johansson, *Phys. Rev. Lett.* **84**, 3638 (2000).
 - [21] D. Alfè, M. J. Gillan, and G. D. Price, *J. Chem. Phys.* **116**, 6170 (2002).
 - [22] J. R. Morris, C. Z. Wang, K. M. Ho, and C. T. Chan, *Phys. Rev. B* **49**, 3109 (1994).
 - [23] L. Koči, R. Ahuja, A. B. Belonoshko, and B. Johansson, *J. Phys.: Condens. Matter* **19**, 016206 (2007).
 - [24] A. B. Belonoshko, L. Koči, and A. Rosengren, *Phys. Rev. B* **85**, 012503 (2012).
 - [25] L. Koči, R. Ahuja, and A. B. Belonoshko, *Phys. Rev. B* **75**, 214108 (2007).
 - [26] J. Bouchet, F. Bottin, G. Jomard, and G. Zérah, *Phys. Rev. B* **80**, 094102 (2009).
 - [27] Y. Usui and T. Tsuchiya, *J. Earth Sci.* **21**, 801 (2010).
 - [28] J. R. Morris and X. Song, *J. Chem. Phys.* **116**, 9352 (2002).
 - [29] D. Alfè, *Phys. Rev. B* **68**, 064423 (2003).
 - [30] S. Root, L. Shulenburger, R. W. Lemke, D. H. Dolan, T. R. Mattsson, and M. P. Desjarlais, *Phys. Rev. Lett.* **115**, 198501 (2015).
 - [31] A. B. Belonoshko and L. S. Dubrovinsky, *Am. Mineral.* **81**, 303 (1996).
 - [32] H. L. Tepper and W. J. Briels, *J. Chem. Phys.* **115**, 9434 (2001).
 - [33] R. Ahuja, A. B. Belonoshko, and B. Johansson, *Phys. Rev. E* **57**, 1673 (1998).
 - [34] A. B. Belonoshko, R. Ahuja, O. Eriksson, and B. Johansson, *Phys. Rev. B* **61**, 3838 (2000).
 - [35] Q.-J. Hong and A. van de Walle, *J. Chem. Phys.* **139**, 094114 (2013).

- [36] Y. Feng, J. Chen, D. Alfé, X.-Z. Li, and E. Wang, *J. Chem. Phys.* **142**, 064506 (2015).
- [37] J. Chen, X.-Z. Li, Q. Zhang, M. I. J. Probert, C. J. Pickard, R. J. Needs, A. Michaelides, and E. Wang, *Nat. Commun.* **4**, 2064 (2013).
- [38] D. A. Young, A. K. McMahan, and M. Ross, *Phys. Rev. B* **24**, 5119 (1981).
- [39] D. Lévesque, J.-J. Weis, and M. L. Klein, *Phys. Rev. Lett.* **51**, 670 (1983).
- [40] P. Loubeyre and J.-P. Hansen, *Phys. Rev. B* **31**, 634 (1985).
- [41] M. Ross and D. A. Young, *Phys. Lett. A* **118**, 463 (1986).
- [42] P. Hohenberg and W. Kohn, *Phys. Rev.* **136**, B864 (1964).
- [43] W. Kohn and L. J. Sham, *Phys. Rev.* **140**, A1133 (1965).
- [44] G. Kresse and J. Hafner, *Phys. Rev. B* **47**, 558 (1993).
- [45] G. Kresse and J. Hafner, *Phys. Rev. B* **49**, 14251 (1994).
- [46] G. Kresse and J. Furthmüller, *Phys. Rev. B* **54**, 11169 (1996).
- [47] G. Kresse and J. Furthmüller, *Comput. Mater. Sci.* **6**, 15 (1996).
- [48] J. Hafner, *J. Comput. Chem.* **29**, 2044 (2008).
- [49] M. Preising, W. Lorenzen, A. Becker, R. Redmer, M. D. Knudson, and M. P. Desjarlais, *Phys. Plasmas* **25**, 012706 (2018).
- [50] S. Nosé, *J. Chem. Phys.* **81**, 511 (1984).
- [51] S. Nosé, *Prog. Theor. Phys. Suppl.* **103**, 1 (1991).
- [52] D. M. Bylander and L. Kleinman, *Phys. Rev. B* **46**, 13756 (1992).
- [53] P. E. Blöchl, *Phys. Rev. B* **50**, 17953 (1994).
- [54] A. Baldereschi, *Phys. Rev. B* **7**, 5212 (1973).
- [55] J. P. Perdew, K. Burke, and M. Ernzerhof, *Phys. Rev. Lett.* **77**, 3865 (1996).
- [56] W. Lorenzen, Phase transitions in hydrogen-helium mixtures, Ph.D. thesis, University of Rostock, 2012 .
- [57] W. Humphrey, A. Dalke, and K. Schulten, *J. Mol. Graph.* **14**, 33 (1996).
- [58] R. A. Evarestov and V. P. Smirnov, *Phys. Status Solidi (b)* **119**, 9 (1983).
- [59] J. Klimeš, D. R. Bowler, and A. Michaelides, *J. Phys.: Condens. Matter* **22**, 022201 (2010).
- [60] W. Lorenzen, B. Holst, and R. Redmer, *Phys. Rev. Lett.* **102**, 115701 (2009).
- [61] W. Lorenzen, B. Holst, and R. Redmer, *Phys. Rev. B* **84**, 235109 (2011).
- [62] B. Monserrat, N. D. Drummond, C. J. Pickard, and R. J. Needs, *Phys. Rev. Lett.* **112**, 055504 (2014).
- [63] H. Niki, H. Nagara, H. Miyagi, and T. Nakamura, *Physics Letters A* **79**, 428 (1980).
- [64] W. B. Hubbard and B. Militzer, *Astrophys. J.* **820**, 80 (2016).
- [65] R. Püstow, N. Nettelmann, W. Lorenzen, and R. Redmer, *Icarus* **267**, 323 (2016); the data for the dotted curve in Fig. 4 were provided by N. Nettelmann.
- [66] P. Bergeron, D. Saumon, and F. Wesemael, *Astrophys. J.* **443**, 764 (1995).
- [67] J. Klimeš, D. R. Bowler, and A. Michaelides, *Phys. Rev. B* **83**, 195131 (2011).
- [68] A. Becker, W. Lorenzen, J. J. Fortney, N. Nettelmann, M. Schöttler, and R. Redmer, *Astrophys. J. Suppl. Series* **215**, 21 (2014).
- [69] F. Simon and G. Glatzel, *Z. Anorg. Allg. Chem.* **178**, 309 (1929).
- [70] V. V. Kechin, *J. Phys.: Condens. Matter* **7**, 531 (1995).